





Article

The Development of a High-Efficiency Small Induction Furnace for a Glass Souvenir Production Process Using Multiphysics

Jatuporn Thongsri ^{1,*}, Piyawong Poopanya ², Sanguansak Sriphalang ³ and Sorathorn Pattanapichai ¹

¹ Computer Simulation in Engineering Research Group, College of Advanced Manufacturing Innovation, King Mongkut's Institute of Technology Ladkrabang, Bangkok 10520, Thailand; sorathorn.pat@gmail.com

² Program of Physics, Faculty of Science, Ubon Ratchathani Rajabhat University, Ubonratchatani 34000, Thailand; piyawong.p@ubru.ac.th

³ Program of Chemistry, Faculty of Science, Ubon Ratchathani Rajabhat University, Ubonratchatani 34000, Thailand; sanguansak.s@ubru.ac.th

* Correspondence: jatuporn.th@kmitl.ac.th

Abstract: A small induction furnace (SIF), which has the important components of copper coils, a ceramic jig, and a graphite crucible, employed for a glass souvenir production process, has been developed as a form of clean technology for multiphysics, consisting of electromagnetics analysis (EA) and thermal analysis (TA). First, two experiments were established to measure parameters for multiphysics results validation and boundary condition settings. Then, the parameters were applied to multiphysics, in which the EA revealed magnetic flux density (B) and ohmic losses, and the TA reported a temperature consistent with the experimental results, confirming the multiphysics credibility. Next, a ferrite flux concentrator was added to the SIF during development. Multiphysics revealed that PC40 ferrite, as a flux concentrator with a suitable design, could increase B by about 159% compared to the conventional SIF at the power of 1000 W. As expected, the B increases alongside the increase in power applied to the coils, and is more densely concentrated in the flux concentrator than in other regions, enhancing the production process efficacy. Lastly, the developed SIF was employed in the actual process and received good feedback from users. The novel research findings are the developed SIF and methodology, exclusively designed for this research and practically employed for a glass souvenir production process.

Keywords: ANSYS Maxwell; clean technology; finite element analysis; glass souvenir; heat transfer; induction heating; magnetic flux concentrator; multiphysics; SDGs; sustainable development goals; thermal simulation; thermochromic dye



Citation: Thongsri, J.; Poopanya, P.; Sriphalang, S.; Pattanapichai, S. The Development of a High-Efficiency Small Induction Furnace for a Glass Souvenir Production Process Using Multiphysics. *Clean Technol.* **2024**, *6*, 1181–1202. <https://doi.org/10.3390/cleantechnol6030058>

Academic Editors: Beatriz Valle and Carolina Montero-Calderón

Received: 20 May 2024

Revised: 30 August 2024

Accepted: 5 September 2024

Published: 9 September 2024



Copyright: © 2024 by the authors. Licensee MDPI, Basel, Switzerland. This article is an open access article distributed under the terms and conditions of the Creative Commons Attribution (CC BY) license (<https://creativecommons.org/licenses/by/4.0/>).

1. Introduction

Induction furnaces are widely used in various industries due to their efficiency, clean technology, usage flexibility, and ability to provide more precise control during the heating process compared to using fuel burning. Some typical applications of induction furnaces include, for example, metal melting, metal casting, heat treatment, forging, brazing, soldering, surface hardening, crystal growing, glass melting, and precious metal refining [1–3].

The induction furnace operation involves magnetic flux density (B) and temperature (T) due to electromagnetic waves and heat transfer. The higher B is, the greater T ; therefore, both B and T are essential parameters to investigate how best to achieve high efficacy in the heating process. Since B and T depend on the induction furnace designs and operating conditions, which require complex experiments to measure, multiphysics, consisting of electromagnetic analysis and thermal analysis, is an alternative tool to determine B , T , and optimization to develop the heating process to suit specific work. For example, Perminov and Nikulin [4] used multiphysics by solving mathematical models of magnetic field diffusion into the melt and convection motion of a conducting paramagnetic liquid in a variable magnetic field, to determine heat and mass transfer and magnetic field diffusion in

an induction furnace. The results obtained by solving mathematical models have limitations in practical applications since this work is based on theoretical study. Multiphysics based on finite element analysis (FEA) was developed as commercial software, such as COMSOL, ANSYS, MSC Software, etc., employed to extend the study of induction furnaces to practical applications more effectively than the mathematical model [4]. For example, multiphysics was employed to estimate B and T in a stepped-diameter crucible by Hadad et al. [5], to investigate the heat transfer and evaporation processes for developing a vacuum induction furnace [6,7], and to study multiphase flow and heat transfer within an induction melting furnace by Buliński et al. [8]. Lu et al. [9] used multiphysics to study titanium melting by a high-frequency inductive heating furnace. Also, multiphysics was applied to develop the vacuum induction melting process by Garcia-Michelena et al. [10], as well as in the study of a microwave kiln and induction heating machine by Jansaengsuk et al. [11,12]. All multiphysics results reported in [4–12] reasonably agree with the experimental results and confirm that B and T are affected by the design and operating conditions of the heating process. Accordingly, many researchers have focused on controlling B and T to suit specific purposes in developing the heating process. Focusing on B in developing the heating process, researchers divided it into three groups: coil, crucible, and magnetic flux concentrator developments.

In the first group of coil development, for example, Stauffer et al. [13] designed five coil shapes for clinical hyperthermia, and they found that for a solenoid coil, B increased alongside the increase in the number of coil turns and applied current. Notably, a double-layer shape, reverse-wound solenoid coil is suitable, controlling B to suit their work. Khazaal et al. [14,15] applied electromagnetic analysis to confirm that the higher the coil's thickness, the lower the B . Also, they found that the higher the frequency, the greater the B . Karnaushenko et al. [16] reported that among the various coil designs, the multilayer solenoid inductor has the best inductance per given piece of wire (GPW). However, resistive loss in the conductor depends on the material and total length. This means the multilayer solenoid inductor is also prone to generating strong fringe fields that may lead to unwanted interference heat on another electronic device. Jansaengsuk et al. [12,17] successfully developed novel coils, as well as single and series-dual coils, to increase manufacturing efficacy for a jewelry factory. They also reported a technique to measure the current (I), frequency (f) applied to the coils, film convection coefficient (h), and temperature (T) of the heating objects. Their technique is simple and practical for setting up simulations.

In the second group, crucible development, Przulucki et al. [18] successfully modified a cold crucible design to improve the melting process efficacy using multiphysics consisting of electromagnetic analysis, thermal analysis, and computational fluid dynamics (CFD). Fashu et al. [19] reviewed and highlighted the progress of state-of-the-art design in crucible design. They concluded that the crucible design for a high-efficacy induction furnace should consider parameters such as crucible–melt interactions, thermodynamic stability, and the thermal shock resistance of different crucibles. Michelena et al. [20] investigated the effect of the crucible composition on the Inconel 718 vacuum induction melting process efficiency. The results can be applied to optimize the melting process in industrial-scale production.

In the last group, the magnetic flux concentrator development, Rudnev and Lovelless [21] reported that it should consist of soft magnetic materials, since they can rapidly change magnetization, affecting the heating temperature. They also suggested the parameters of the magnetic flux concentrator to improve the heating process. Since one of the major problems obstructing the induction furnace development is the proximity effect resulting from two adjacent coils with different current directions, Nian et al. [22] successfully solved this problem using the magnetic flux concentrator and magnetic shielding induction. They also reported that the ferrite is a suitable shielding material, since it can effectively control magnetic fields in the desired direction if appropriately designed and can not be heated by the induction coil. Im et al. [23] studied the effect of the ferrite core in the induction range and proposed a design for efficiency improvement. Since ferrite is the magnetic material,

and the induction range working relies on electromagnetic analysis, their results will benefit the design of a magnetic flux concentrator for a new generation of induction furnaces.

Small and medium enterprises (SMEs) are another Thai business sector that is important as a driving force for the economy. Most of them come from the grassroots and are low-income people pursuing business. In 2022, Thai SMEs produced 35% of the gross domestic product (GDP), about 103.8 billion USD. Unfortunately, they constituted 71% of employment [24], implying that the current production process is still outdated since it uses a lot of labor but generates little income, leading to little GDP. Accordingly, novel processes and technology development are solutions to reduce labor use and increase income, helping Thai SMEs.

This article reports on the successful development of a glass souvenir production process at a Thai SME factory as a case study. This factory is in the Ubonratchathani province, the northeastern region of Thailand, producing glass souvenirs to sell to local tourists. One of the essential processes for producing the glass souvenir is the glass melting, using a small induction furnace (SIF) as a conventional model. Figure 1 shows the sample of (a) a glass souvenir and (b) a small induction furnace used to melt the recycled glass scraps, the raw material for producing the glass souvenir depicted in (a). According to the literature review mentioned above and the discussion with the factory, the authors concluded that preparing souvenirs as a thermochromic dye and developing an SIF using multiphysics to achieve high-efficiency glass souvenir production are keys to increasing income and helping Thai SMEs.

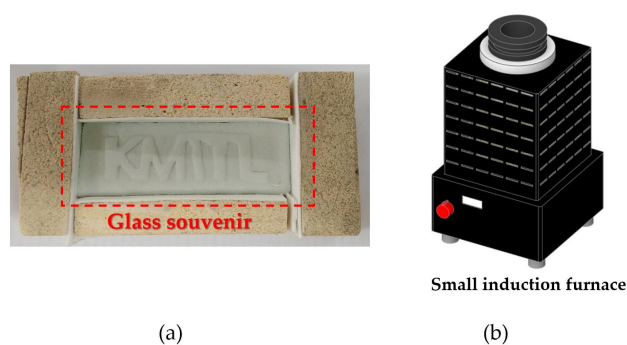


Figure 1. The sample of (a) a glass souvenir and (b) a small induction furnace for a glass souvenir production process.

In this article, we focus on developing SIF by adding a suitable shape of the flux concentrator to enhance B , since it strongly influences B over coils and crucibles. First, the glass souvenir production process was investigated to determine essential parameters, I , f , h , and T , that impacted the melting process of SIF. These parameters were employed later for multiphysics settings and results validation. Next, the SIF was set in a laboratory based on the actual condition, and essential parameters were measured. Then, multiphysics was employed to investigate B and T . Finally, the simulation results were validated and analyzed to determine the novel design of SIF, which is practical and can enhance the production process efficiency.

The novel aspects of this research include a new design of SIF and an improved glass souvenir production process developed by multiphysics, obeying SDGs 9 and 12. Multiphysics results revealed the T and B , consistent with the experimental results and previous works. Therefore, the research methodology is credible and can be applied further in developing other induction heating devices.

2. Theoretical Background

As described in Section 1, the keys to success in helping Thai SMEs are a thermochromic dye souvenir and a high-efficiency SIF developed by multiphysics. The theoretical background and governing equations are summarized as follows.

2.1. Glass Souvenir Production Process

Figure 2 shows the glass souvenir production process, which includes raw material preparation, weighing, mixing, melting, forming, inspection, decoration, and packing. The melting and decoration processes are highlighted in this research in blue, since both are key to increasing Thai SMEs' income.

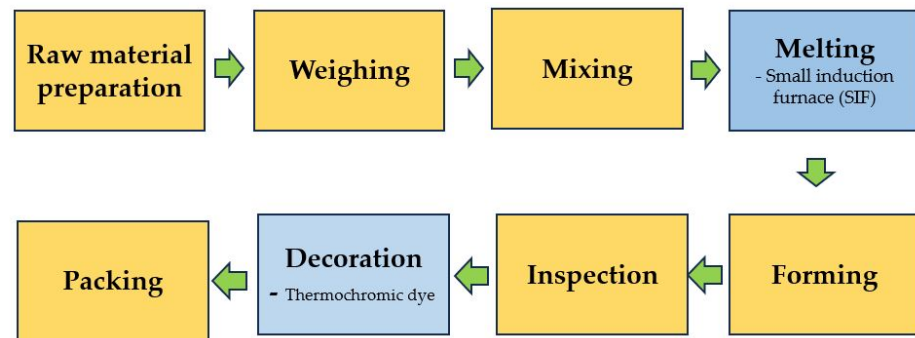


Figure 2. The glass souvenir production process.

2.1.1. Raw Material Preparation

This Thai SME factory used recycled glass scraps to earn a high income and preserve the environment as a clean technology. Household glass scraps were cut to the proper size, cleaned, and prepared for the following process as raw materials.

2.1.2. Weighting

The raw materials were weighed to reach a specific value depending on the glass souvenir design, awaiting the next process.

2.1.3. Mixing

After weighting, soda ash or sodium carbonate (Na_2CO_3) was added to the raw materials. The soda ash lowers the melting temperature and helps the melting glass form a new shape easily. If the factory wants the souvenir to be strong and durable, calcium carbonate (CaCO_3) is filled into the raw materials. Then, the chemicals and raw materials are mixed together, and the mixture is called a batch.

2.1.4. Melting

Then, the batch was poured into a container and placed in the crucible of SIF. When the SIF operates, the batch will melt, becoming melting glass because of the heating generated based on multiphysics, described in Section 2.2. The melting process is the most important. If the heat is insufficient enough to melt the batch, the products will have defects, and the process will not be efficient. As mentioned in Section 1, the literature review indicates that the development of SIF leads to a high-efficacy process; therefore, it is the aim of this research. Moreover, since the SIF uses electricity, not charcoal or oil, this process also qualifies as clean technology.

2.1.5. Forming

The melting glass was removed from the SIF and filled into the mold and the blocks. The blocks around the glass souvenir, for example, are shown in Figure 1a. The mold was designed to be modern and attractive to the customers. After that, the melting glass was cooled down, forming a colorless glass souvenir. For example, in Figure 1a, the mold is a rectangular block with a King Mongkut's Institute of Technology (KMUTL) logo. Importantly, the mold should not be larger than the crucible.

2.1.6. Inspection

All colorless glass souvenirs were inspected for quality control to investigate defects, such as cracks, fractures, imperfect shapes, etc. If there were defects, the products were rejected and returned to recycled materials again.

2.1.7. Decoration

The products that passed from the previous process were painted in color and decorated with beautiful accessories during this process, to attract customers. Notably, Figure 1a shows a sample product employed to simply present the glass souvenir production process; therefore, it is neutral and would not be considered gorgeous by some readers, avoiding copyright problems. In the actual process of Thai SME factories, the product designs are absolutely modern and attract customers. One of the keys to attracting customers is making glass souvenirs with thermochromic (TC) dyes that change color with temperature variations. The TC dyes are sensitive to temperature changes and can transition between two or more colors depending on the temperature they are exposed to. The TC dyes work based on a principle where their molecular structure changes in response to temperature, altering the way they absorb and reflect light, thus resulting in a change in color. This property makes them useful in various fun customer-facing and practical applications.

We prepared an orange-yellow thermochromic dye, which was painted on the glass. This process was modified from the successful work of Sripalang et al. [25] in preparing thermochromic dye to suit the actual operating conditions of Thai SMEs. The orange thermochromic dye (OTC) 0.13 g, 0.24 mmol; Bis-phenol A (BPA) 0.33 g, 1.44 mmol; and Octadecanol (OD) 6.49 g, 24 mmol were mixed. The solid phase thermochromic system was prepared by stirring 0.13 g of TC, 0.33 g of BPA, and 6.49 g of OD at 60 °C for 1 h. After cooling down, TC was obtained, with orange solids. After the thermochromic pigment is obtained, it is mixed with solutions of naphtha xylene, butyl acetate, acrylic resin, hardener, and a thinner to form a color solution, then coated on the glass surface and tested for thermal properties. In addition, digital photography was used to evaluate the effect of temperature changes on color. A TC glass on a hot plate was utilized in the methodology. After reaching the desired temperature, the samples were removed from the hot plate, and an image was recorded using a digital camera. The trend in TC color difference variations based on temperature changes from 40 to 70 °C is shown in Figure 3. The color of TC changed from orange to yellow as the temperature increased. The color changed significantly when the painted TC glass was heated to 60 °C. Figure 3 shows a sample of a glass souvenir prepared with a thermochromic dye.

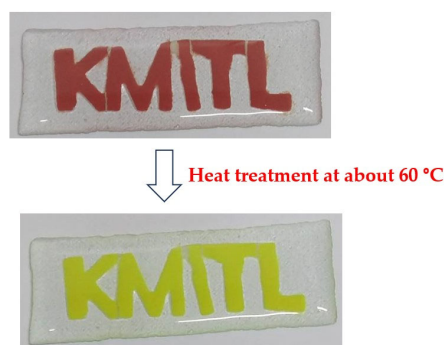


Figure 3. A sample of a glass souvenir prepared with a thermochromic dye.

2.1.8. Packing

Finally, the glass souvenirs were put into the packaging and sold to a store.

2.2. Induction Heating in the SIF

It briefly describes principles related to heat generation in the SIF, including essential parameters for analysis. When the alternating current (I) with frequency (f) is applied to

the coil, magnetic flux density (B) is generated based on a principle governed by Maxwell's equations. Since the B is inversely proportional to distance, the maximum magnetic flux density (B_{max}) is on the coil's surface, and the B is reduced due to being at a distance farther from the coil. B_s is on the crucible surface. Then, B generates the heat inside the crucible based on Joule's heating effect, skin-depth effect, proximity effect, slot effect, and heat transfer principles. The higher the I , the greater the B . The higher the B , the greater the T . Figure 4 shows the induction heating in the SIF consisting of copper coil, ceramic jig, and graphite crucible. Glass is a non-conductive material, and the SIF melts glass through indirect heat generation. The graphite crucible induces conductive material, transferring the characteristics of heat and melting to the glass. Please note that B_s is focused on the results of developing the SIF.

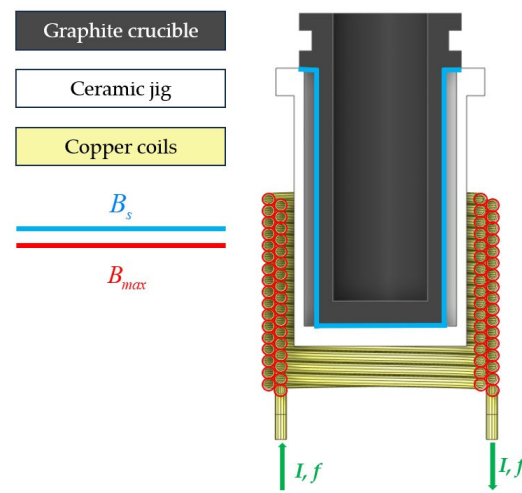


Figure 4. The induction heating in SIF.

Multiphysics is a proper tool for investigating the B and T inside the SIF. Its principles and governing equations were clearly explained in detail by the work of Jansaengsuk et al. [12,17]; however, the brief is explained in Section 2.3, detailing multiphysics.

2.3. Principle of Multiphysics

It includes principles of electromagnetics, Joule's heating effect, skin effect, heat transfer, and magnetic flux concentrator.

2.3.1. Maxwell's Equation

In electromagnetics, the B generated by the coils can be determined by solving Maxwell's equations given by [12,17]

$$\nabla \cdot \mathbf{E} = \frac{\rho_v}{\epsilon} \quad (1)$$

$$\nabla \cdot \mathbf{H} = 0 \quad (2)$$

$$\nabla \times \mathbf{E} = -\mu \frac{\partial \mathbf{H}}{\partial t} \quad (3)$$

$$\nabla \times \mathbf{H} = \mathbf{J} + \epsilon \frac{\partial \mathbf{E}}{\partial t} \quad (4)$$

where ρ_v is the volume electric density, \mathbf{J} is the electric current density, ϵ is the permittivity, μ is the permeability, \mathbf{E} is the electric field, and \mathbf{H} is the magnetic field. Equations (1)–(4) are known as Gauss's law for the electric, Gauss's law for magnetism, Faraday's law, and Ampere's law, respectively. Notably, bold letters refer to vectors.

In the simplest case, with a circular coil of distance d from the center with N turn, the B at the center can be calculated by Biot–Savart’s law, expressed by [12,17]

$$\mathbf{B} = \frac{\mu_0 N I}{2d} \quad (5)$$

where μ_0 is the permeability of free space, and I is the applied current to the coil.

As seen in Figure 4, the SIF consists of hollow double-layer coils with many turns; therefore, the simple Equations (1)–(5) are insufficient to determine B , requiring electromagnetic analysis.

2.3.2. Joule’s Heating Effect

The governing equation of Joules heating is given by [12,17]:

$$P = I_d^2 R \quad (6)$$

where P is the power, I_d is the eddy current, and R is the coil’s resistance.

2.3.3. Skin Effect

The skin effect occurs due to the generation of eddy currents within the conductor, which create magnetic fields opposing the original current. The opposition is more vigorous in the center of the conductor, forcing the current to flow more on the surface. Therefore, the heat prefers to distribute on the outer surface at a distance not greater than δ , called the skin depth, expressed by [12]

$$\delta = \sqrt{\frac{\rho_r}{\pi f \mu}} \quad (7)$$

where ρ_r is the electric resistivity, f is the frequency, and μ is the magnetic permeability.

2.3.4. Heat Transfer

The heat in the outer surface from the skin effect transfers to the inner surface based on the heat transfer principle. It can be calculated by [12]

$$\rho_m C_p \frac{\partial T}{\partial t} - k \nabla^2 T = Q \quad (8)$$

where ρ_m is the mass density, k is the conductivity, C_p is the specific heat capacity, T is the temperature, Q is the volumic power density or the internal heat source, and t is the time.

Additionally, the convection and radiation are governed by [12]

$$k \nabla T \cdot \hat{n} + h(T - T_{amb}) + \varepsilon \sigma_{sb} (T^4 - T_{amb}^4) = 0 \quad (9)$$

where h is the convection coefficient, \hat{n} is the normal unit vector, ε is the material emissivity, and σ_{sb} is the Stefan–Boltzman constant. The subscription *amb* is for the ambient value.

2.3.5. Flux Concentrator

A flux concentrator in magnetics is a component used to enhance or redirect magnetic flux in a particular direction within a magnetic circuit. It is commonly used in applications where efficient flux management is crucial, such as transformers, inductors, electric motors, magnetic sensors, and induction heating devices. Flux concentrators are typically made from materials with high magnetic permeability, such as soft magnetic alloys like ferrite, iron, or certain types of steel. These materials facilitate the concentration of magnetic flux lines, directing them through desired paths and reducing losses. There are several types of flux concentrators, including magnetic cores, shields, flux guides, and yokes.

- Magnetic cores are commonly used in transformers and inductors to channel and concentrate magnetic flux generated by coil windings. Magnetic cores can be in the form of laminated iron or steel sheets, ferrite cores, or powdered iron cores.
- Magnetic shields are used to confine or redirect magnetic fields, protecting sensitive components from magnetic interference. Magnetic shields can be made from high-permeability materials like mu-metal or Permalloy.
- Magnetic flux guides are structures that guide magnetic flux to specific regions within a device or system. They are often used in magnetic sensors and actuators to enhance performance and sensitivity.
- Magnetic yokes are components that complete a magnetic circuit by connecting the ends of a magnetic core or flux concentrator. Yokes help to minimize magnetic leakage and improve the efficiency of magnetic devices.

Overall, flux concentrators play a crucial role in optimizing the performance and efficiency of magnetic systems by managing the distribution of magnetic flux and minimizing losses.

The selection of a flux concentrator should be based on various factors, such as relative permeability, resistivity, curies point, saturation flux density, and power loss. The permeability and resistivity of flux concentrators have the most effect on the efficiency and performance of induction heating systems. Whenever the temperature and the B of the flux concentrator play a role over the curies point and over flux saturation, ferromagnetic material becomes non-ferromagnetic. It cancels the magnetic properties of the flux concentrator. These factors must be evaluated to select and design the flux concentrator and determine the suitable material and size.

In sum, multiphysics simulation is the computational modeling and analysis of physical phenomena involving multiple interacting physical processes or fields. In other words, it involves simulating systems where more than one type of physical phenomenon is present and they interact with each other. For the SIF in this work, multiphysics, which consists of electromagnetics and thermal analysis, was presumed to cover electromagnetics, Joule's heating effect, skin effect, heat transfer, and magnetic flux concentrator principles.

In ANSYS Maxwell, the electromagnetic analysis software v. 2021R1 covers the Maxwell, Joule's heating and skin effect problems of (1)–(7) based on the finite element method governed by [12,17,26]

$$[S][H] = [J] \quad (10)$$

where $[S]$, $[H]$, and $[J]$ are the stiffness, magnetic field, and electric current density matrices, respectively.

In ANSYS steady-state thermal analysis v. 2021R1, the software covers the heat transfer in Equations (8) and (9) based on the finite element method [27,28] by

$$[K]\{T\} = \{Q\} \quad (11)$$

where $[K]$ is the thermal stiffness matrix, $\{T\}$ is the nodal vector temperature, and $\{Q\}$ is the external-thermal vector load.

When adding a magnetic flux concentrator into the models, changing material properties, or redesigning the models, Equations (10) and (11) are modified. Multiphysics solves Equation (10) to determine B and ohmic losses (ΔV_{Ohm}) for setting the boundary conditions of thermal analysis, and then it solves Equation (11) to determine the T employed for analysis.

3. Methodology

This section describes the research methodology involving conventional SIF, the experiment set to determine essential parameters for the simulation, and multiphysics for SIF development. Figure 5 shows the research methodology flowchart. The experiments and multiphysics are colored blue and yellow, respectively.

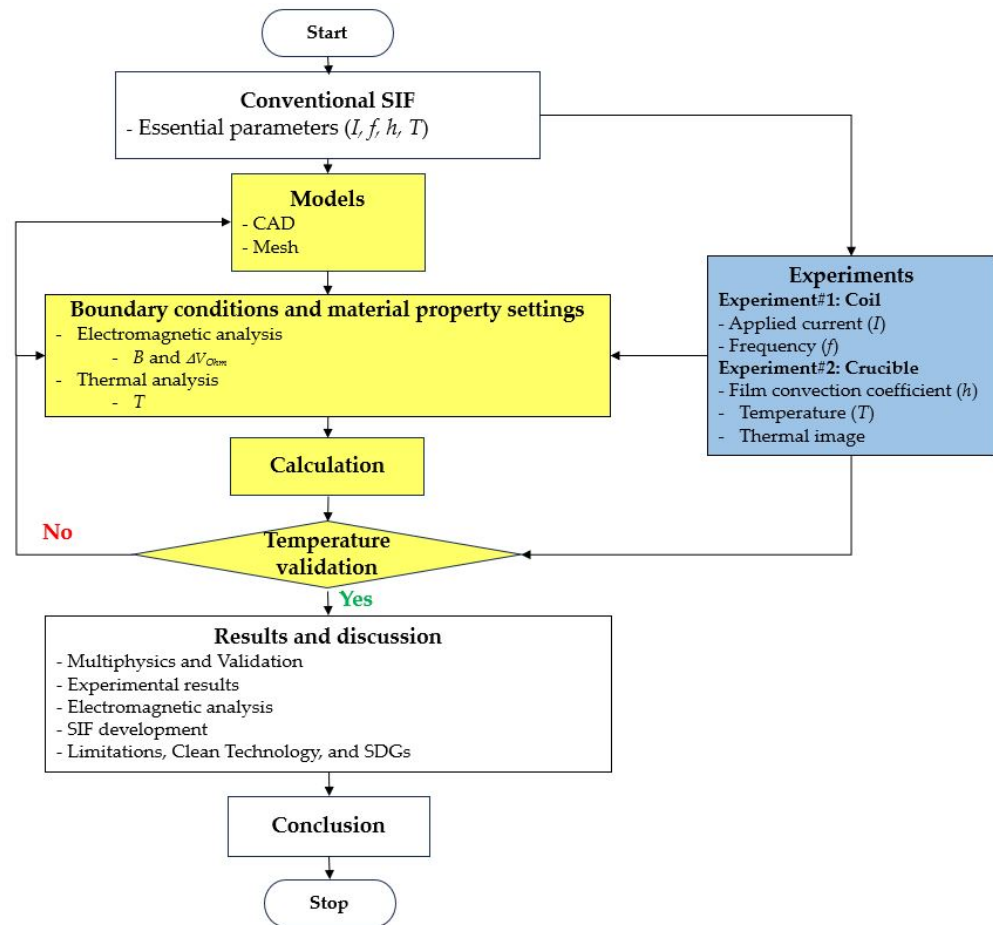


Figure 5. The research methodology flowchart.

3.1. Conventional SIF

The authors studied the production in the factory, explained in Sections 2.1.1–2.1.8, especially the SIF presented in Figure 1b, to establish the experiment in a laboratory and model for simulation. Figure 6 presents the conventional SIF model and material components used for multiphysics simulation by ignoring irrelevant components. This type of SIF is widely used in Thai SME factories since it is cheap, small, convenient to move, easy to maintain, and can generate a maximum temperature of about 2000 °C; therefore, it was selected as a case study. Induction heating occurs inside the crucible, where the ceramic jig, copper coil, and crucible graphite function together, as described in Section 2.2. The metal cover functions as the main structure containing all components, including the electrical circuit and controller. The copper coils are hollow, allowing cooling water to flow in and out, reducing the coils' temperature to a constant of 25 °C.

With the results of studying the SIF to mimic the glass souvenir production process, the authors found that essential parameters for the experiments and multiphysics are applied current to the coil (I), frequency (f), film convection coefficient (h), and temperature (T). The first two parameters, I and f , are for boundary condition settings in electromagnetic analysis, and the others, h and T , are for boundary condition settings in thermal analysis. Therefore, two experiments were set to measure the parameters mentioned, which are described next.

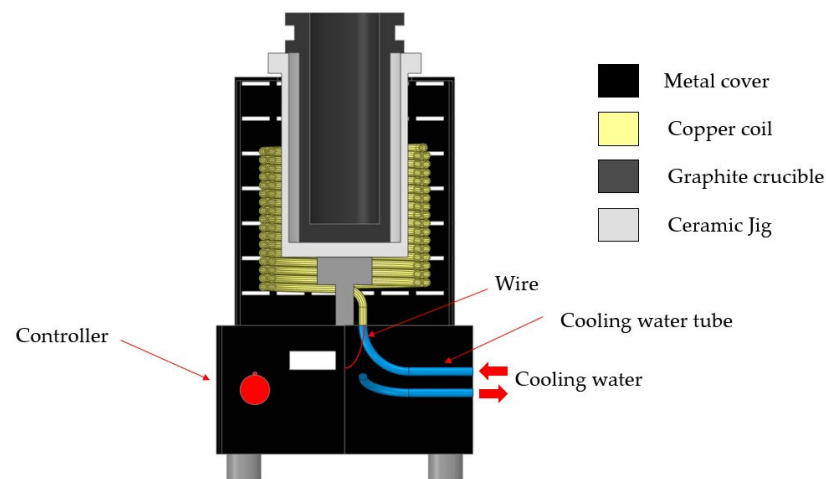


Figure 6. The conventional SIF and material components.

3.2. Experiments

Two experiments presented in Figure 7 were set to measure I , f , h , and T for the SIF power varying from 1000 W to 2200 W. Both were modified from previous experiments proposed by Jansaengsuk et al. [12,17], which successfully developed the induction heating machine for jewelry factories, based on the same principle as the SIF. The experiments were explained accordingly.

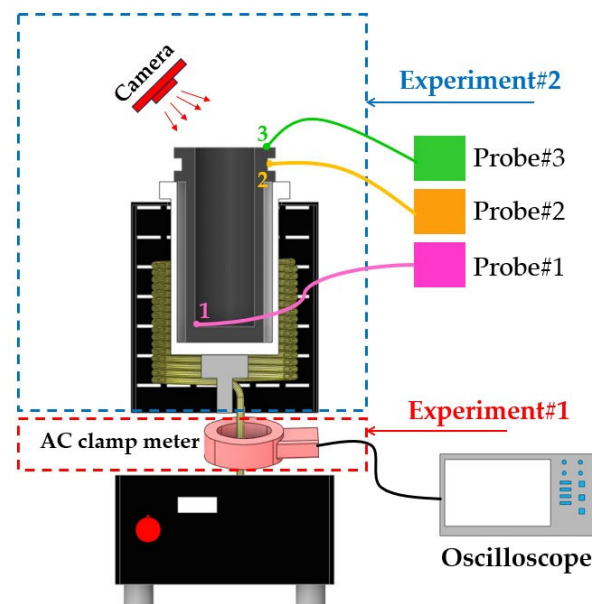


Figure 7. The setup experiments.

3.2.1. Experiment #1

This experiment was designed to measure I and f applied to the coils using an AC clamp meter (APC 100). The AC clamp meter was connected to an oscilloscope (Tektronix TBS 1072B-EDU). The signals displayed on the oscilloscope were analyzed to determine I and f . The experimental results will be reported the next section.

3.2.2. Experiment #2

This experiment was designed to measure h and T , including the behavior of increasing the crucible temperature, using a camera and 3-channel thermocouple with probes. A Canon EOS 1000D DSLR camera with 10.1 megapixels, 7-point automatic focusing, 3 frames

per second, and a Lens 1.6x captured the heating of the SIF for 20 min to record the transient behavior of increasing T . The three probes, Probe #1, Probe #2, and Probe #3, measured T at positions 1, 2, and 3, respectively. The accuracy of probes and a thermocouple is $\pm 2\%$ at the maximum T of 1300 °C. The results of T are derived directly from the thermocouple monitor display, while the h is from derived the comparison with thermal analysis results. The experimental results in this section will be reported in the next section.

3.3. Multiphysics

Multiphysics follows the methodology flowchart in Figure 5, explained below.

3.3.1. Models

- CAD model

Figure 8 shows a CAD model with the dimensions for the (a) coils, (b) ceramic jig and graphite crucible, and (c) the SIF after assembling all components. The SIF has double-layer coils. All components in (a) and (b) are vital to the melting process and are essential for multiphysics. The smaller illustration in (a) presents the copper coil's dimensions, which has a diameter of 4.4 mm with 0.5 mm of thickness.

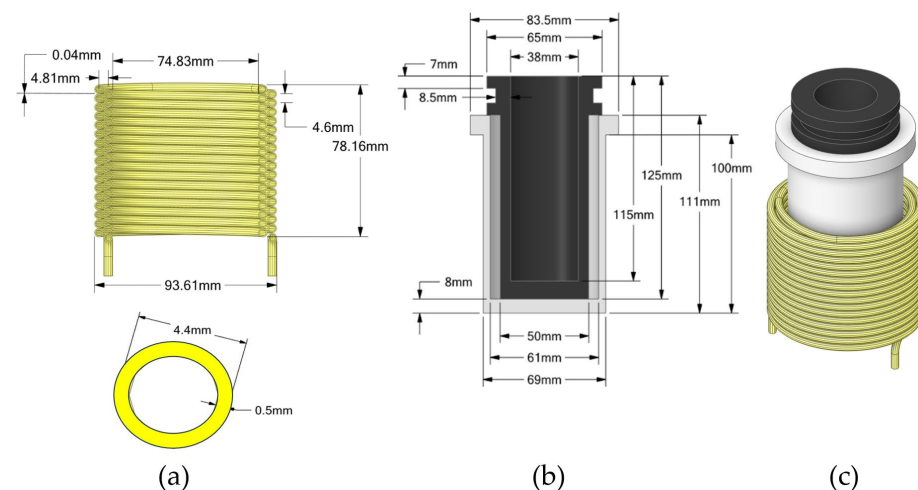


Figure 8. The CAD model with dimensions for (a) coils, (b) jig and crucible, and (c) SIF.

- Mesh model

Figure 9 presents the mesh model. The first mesh model has 0.475 million elements and tetrahedrons. Using the adaptive mesh refinement capability with six passes, the last mesh model adapted from the first model increased to 1.8 million elements with an energy error of less than 0.06% at a converged solution. Significantly, for the first mesh model, the sizing in the coil is the roughest at 9 mm, and the mesh sizing in air space is the largest at 50 mm, while in the last mesh model, after finishing the adaptive mesh refinement, they were 0.06 mm and 0.16 mm, respectively. The last mesh model, using finished adaptive mesh refinement, is suitable for this research after comparing it with the experimental results, since it provides reliable results within our limited time and computational resources. Adaptive mesh refinement is a computational technique used in numerical simulations. It involves dynamically adjusting the resolution of a computational mesh based on the solution characteristics to capture the important features of the problem being simulated efficiently [29], which is suitable for this research.

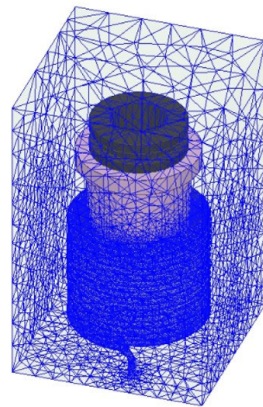


Figure 9. Mesh model.

3.3.2. Boundary Conditions and Material Property Settings

The settings are divided into two steps: electromagnetic and thermal settings.

- Electromagnetic setting

Figure 10 shows the electromagnetic setting of the coils. The I and f results from Experiment #1 were defined at the coils' end. Table 1 reports the I and f collected from Experiment #1 for the SIF power from 1000 W to 2200 W. Importantly, the power and I increase with the decrease in f , as expected, consistent with the work of Jansaengsuk et al. [12,17] in the development of induction heating machine, confirming the credibility of our experiments. Table 2 reports the material property setting. Since k and c of the crucible graphite depend on temperature, the details of the material properties are reported in Table 3.

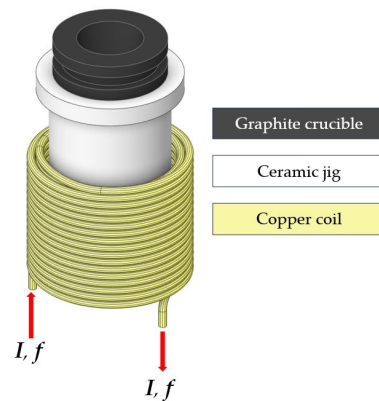


Figure 10. The boundary conditions and material property settings for electromagnetic analysis.

Table 1. The experimental results for electromagnetic setting.

Power (W)	I (A)	f (kHz)
1000	223.93	27.92
1200	244.79	27.11
1400	269.91	26.50
1600	297.35	25.56
1800	328.62	24.55
2200	377.76	23.11

Table 2. Material property for multiphysics settings.

Material	ϵ_r	k_r	σ (S/m)	ρ (kg/m ³)	k (W/m °C)	c (J/kg °C)
Ceramic jig *	9.8	1	0	3960	45	880
Crucible graphite *	1	1	218,670	2229.8	Table 3	Table 3
Copper coil *	1	0.99991	5.80×10^7	8933	400	385
Air *	1.0006	1.0000004	0	1.16	0.03	1000
Ferrite B **	1	5000	0.9976	4800	N/A	N/A
Ferrite PE22 **	1	1800	3.33×10^{-1}	4800	N/A	N/A
Ferrite PC40 **	1	2300	1.54×10^{-1}	4800	N/A	N/A

* Data from [12,17]. ** Data from [30,31].

Table 3. Material property for crucible graphite [32].

Temperature (°C)	k (W/m °C)	c (J/kg °C)
300	122	1360
500	90	1620
700	72	1785
900	60	1880
1100	52	1955
1300	48	2005

In addition, the material properties of ferrite materials in Table 2 are for magnetic flux concentrator settings, ignoring the thermal property; the results of the varying flux concentrator material grades will be discussed in Section 4.4, detailing the development of the SIF. Codes B, PE22, and PC40 are material grades with different compositions between manganese (Mn) and zinc (Zn) that are named for commercial sale. Not applicable (N/A) means that there is no need to set these values in the software.

After finishing the electromagnetic computation, the results reported B and ΔV_{Ohm} , which were employed to determine h for the thermal setting explained below.

- Thermal setting

The h is a critical value to be defined for calculating T in thermal analysis. This is challenging, since the h cannot be determined from the literature review. In this research, the authors employed the same technique proposed in [11,12,17], briefly explained as follows:

First, the B results on the crucible were converted to ΔV_{Ohm} and were assigned to the crucible. Then, the T measured from Probe #3 in Figure 7 was assigned to the boundary condition. Next, using thermal simulation, the results of T on the crucible were compared with the results of Experiment #2. Lastly, the thermal simulation was repeated until the T results from the simulation and Experiment #2 were consistent and the h was determined. Please see Figure 5 to help with the explanation.

From the comparison between T from the thermal simulation and Experiment #2, the authors found that the crucible should be divided into four zones for four h levels to obtain accurate T . Figure 11 shows the zones for the h of the thermal setting. Table 4 reports h versus the power applied to the coils, determined from the comparison between thermal analysis and Experiment #2, suitable for this research.

Additionally, the one of the reasons behind the zone division is that a ceramic jig and coils cover Zone 1; hence, the effect of convection is the least, and B is the strongest. On the other hand, Zone 4 is outside the ceramic jig and coils (seen in Figures 6 and 7), so the effect of convection is higher, and the effect of B in Zone 4 is the lowest. Therefore, the setting in Figure 11 and Table 4 is appropriate and reasonable.

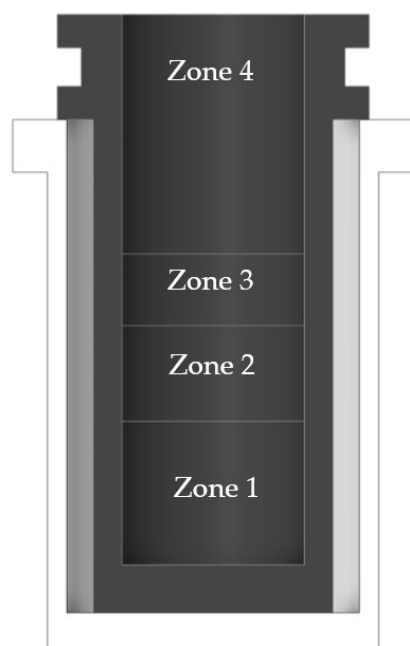


Figure 11. Zones on the crucible for thermal setting.

Table 4. The film convection coefficient (h) for the thermal setting.

Power (W)	h ($\text{W}/\text{m}^2 \text{ } ^\circ\text{C}$)			
	Zone 1	Zone 2	Zone 3	Zone 4
1000	3200	3000	500	10
1600	5500	4000	650	10
2200	6500	4300	700	10

The multiphysics simulation was repeated until the simulation results were consistent with the experiments to confirm multiphysics' credibility, and then all results were analyzed to develop the SIF.

4. Results and Discussion

This section includes validation, multiphysics results, SIF development, limitations, clean technology, and SDGs. The glass souvenir was not included in the model for easy analysis since the authors focused on the SIF development.

4.1. Multiphysics and Validation

Figure 12 shows the results from (a) Experiment #2 by the camera and (b) multiphysics to validate the multiphysics results at 1000 W of the SIF, 1080 s after starting, approaching a steady state analysis.

In a qualitative validation, both results are consistent and reveal that the T inside the crucible was the highest at the bottom, moderate at the middle, and the lowest at the top, as expected, since the bottom of the crucible is in the coils' center; hence, B is the highest and decreased away from the coils' center, consistent with the report by Janseangsuk et al. [12,17]. Moreover, Figure 12a shows that the temperature was divided into at least four levels, underscoring why the crucible in Figure 11 was divided into four zones. In addition, the authors found that Figure 12a cannot be taken with a standard thermal camera and an infrared thermometer because heat and electromagnetic fields interfere with both instruments. Hence, the T measured by the thermal camera is incorrect, implying that only the experiment cannot investigate the temperature distribution inside the crucible, but multiphysics can, as seen in Figure 12b.

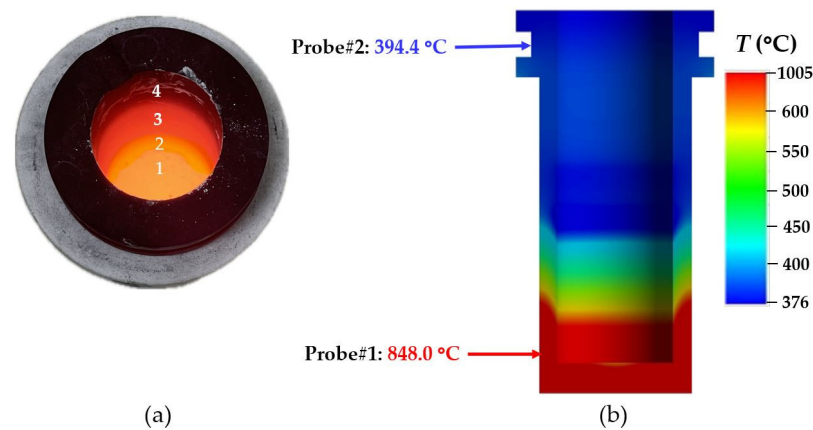


Figure 12. The temperature inside the crucible: (a) captured by the camera and (b) calculated by multiphysics.

In a quantitative validation, Table 5 reports T from Experiment #2 measured by three thermocouple probes (see the probe's positions in Figure 7) and calculated by multiphysics.

Table 5. Temperature measured by thermocouple's probes from Experiment #2 and calculated by multiphysics.

Power (W)	Probe#1 (°C)			Probe#2 (°C)			Probe#3 (°C)		
	Exp.	Mul.	Error	Exp.	Mul.	Error	Exp.	Mul.	Error
1000	820.0	848.0	3.4%	392.7	394.4	0.4%	378.1	378.1	0.0%
1600	1051.1	1037.6	1.3%	466.3	473.9	1.6%	463.0	463.0	0.0%
2200	1250.1	1201.9	4.0%	636.2	581.5	8.6%	549.7	549.7	0.0%

Table 5 confirms that the experimental and multiphysics results are consistent as expected. For example, the multiphysics results reveal in Figure 12b that the temperatures (T) in Probes 1 and 2 were 848.0 °C and 394.4 °C, respectively, at a power of 1000 W, while the experimental results were 820.2 °C and 392.7, which were 3.4% and 0.4% of errors, respectively. The maximum error of the multiphysics result is 8.6% compared to the experimental result at a power of 2200 W. As expected, temperatures from both methods increased with the increase in the power of SIF. Significantly, there is an error of 0.00% in Probe #3, since the temperature in this position was employed as the boundary condition; therefore, both T are equal, as mentioned in Section 3.3.2, as also expected. In addition, since the authors used a normal camera to capture T , resulting in Figure 12a, the thermal setting was divided into four zones, as shown in Figure 11. If we used a high-resolution camera, the T distribution with color level may be clearer than Figure 12a. Thus, the number of zones will increase according to the color level, reducing the error and leading to more accurate simulation results.

Figure 12 and Table 5 confirm that the multiphysics results and the research methodology employed in this research are reliable. However, multiphysics has difficulty calculating T since it requires h from computation, thus needing T measurement and transient state thermal simulation to determine accurate T ; therefore, it causes difficulties and inconvenience. To avoid difficulties and inconvenience, some researchers successfully employed electromagnetic analysis to develop induction heating devices [11–14,17] and enhanced their performance using B as a critical parameter for focusing and considering.

4.2. Electromagnetic Analysis (EA)

Figure 13 shows B (a) around the coils and (b) on the crucible surface as B_s , calculated by EA at the power of 2200 W. Compared to Figure 4, B_{max} was 0.2081 T, while B_s was 0.1439. As expected, the B is the strongest around the coils and decreases with distance from

the coils. Significantly, the maximum B_s was near the crucible bottom in Zone 1 because this position is the coils' center, consistent with the report by Jansaengsuk et al. [12,17]. The crucible top in Zone 4 has a weak B_s because it is not in the coils, as expected. Therefore, this SIF has been effectively designed by the manufacturer. Importantly, the crucible bottom is the best for melting the glass souvenir since it has a high B , leading to the highest T , while the upper is worse since it has a low B , leading to the lowest T . However, the flux concentrator is one of the alternative ways to increase B for the SIF development.

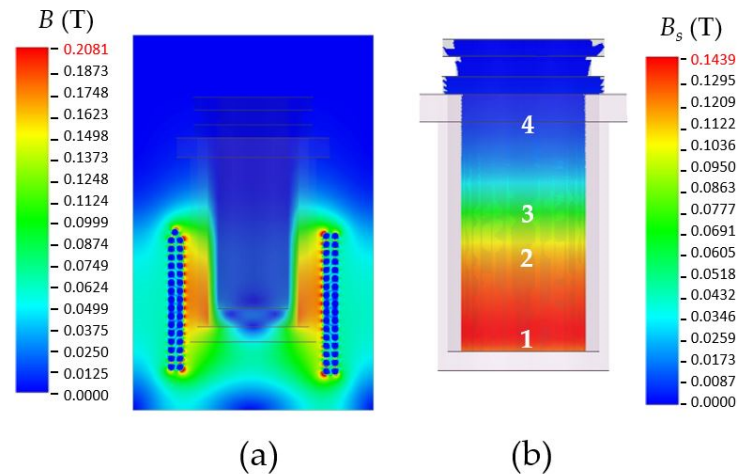


Figure 13. The magnetic flux density (B): (a) around the coils and (b) on the crucible surface.

4.3. SIF Development

This section explains the method for developing SIF to achieve higher efficacy using a flux concentrator and EA.

Ferrite B (Mn-Zn) is a specific ferrite material composed primarily of manganese–zinc (Mn-Zn). This composition commonly produces ferrite cores and other magnetic components [33], specifically flux concentrators. Its advantages are high saturation magnetization, good frequency characteristics, low losses, and high resistivity; therefore, it is suitable for a case study. The Ferrite B was added to the SIF with a cylindrical shape called Model I and dimensions of 5 mm thickness, as shown in Figure 14a. The B_s results calculated by the EA at the power of 2200 W after adding the Ferrite B are presented in Figure 14b, noting that the dimensions were designed to match the conventional design of SIF.

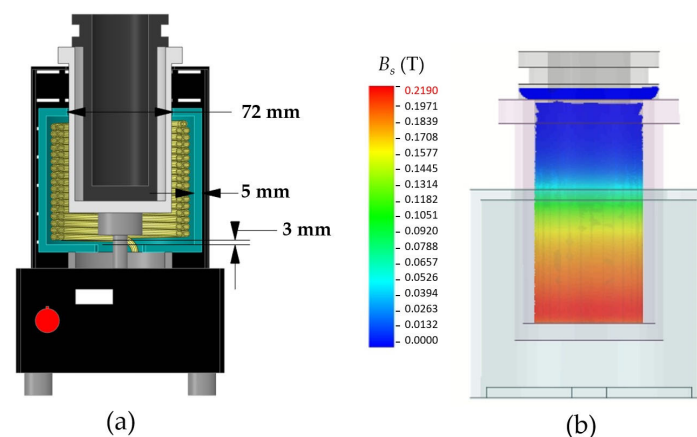


Figure 14. (a) Dimensions of Ferrite B (Mn-Zn) and (b) B_s calculated by EA.

Compared Figure 14b to Figure 13b, the maximum B_s increased from 0.1439 T to 0.2190 T, showing an increment of about 52% because of Ferrite B. As expected, Ferrite B can help enhance B under the same operating conditions.

To determine the effect of flux concentrator shape on B and why B_s in Figure 14b is enhanced compared to Figure 13b, Figure 15 shows B inside the Ferrite B for (a) Model I and (b) Model II. The small adjacent pictures present solid models of the Ferrite B shapes. For Model I, in (a), Ferrite B is a closed cylindrical shape covering all coils, while for Model II in (b) Ferrite B is also cylindrical, but without a top and bottom cover. Compared to the B results in the same color scale, Model I has more potent B than Model II since Model I has top and bottom covers, as expected; therefore, Figure 15 confirms that flux concentrator shape affects B inside SIF. The strongest B is notably found in Ferrite B, since it is the flux concentrator mentioned in Section 2.3.5, as also expected. In addition, the proper shape of the flux concentrator will produce a higher B . After trying many shapes of Ferrite B, the authors found that Model I is suitable for the SIF as a flux concentrator shape.

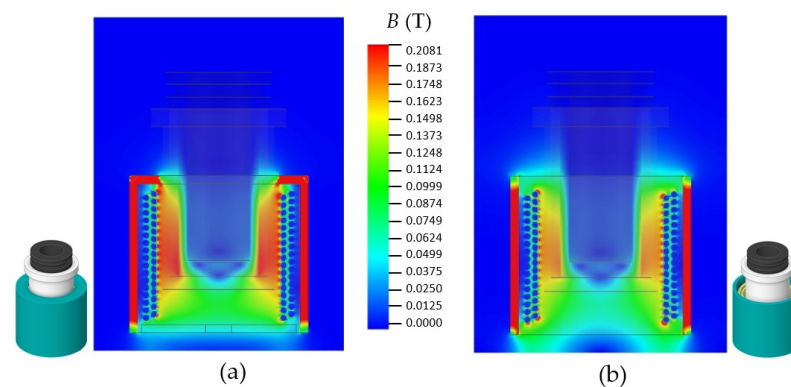


Figure 15. The B inside the Ferrite B for (a) Model I and (b) Model II.

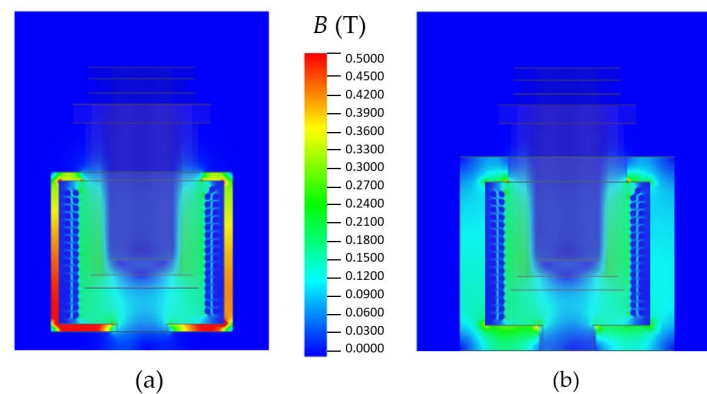
To determine the effect of ferrite types on B , using Table 2, Model I and the EA, the authors found that ferrites B, PE22, and PC40 provided nearly the same maximum B_s , which is about 0.219 T. We expect that the reason why the B_s is the same is due to the small size of SIF or the application of low f . The B_s results would be more significant if the SIF were bigger in size, as in Liu et al.'s work [34]; the flux concentrator for the circular electron-positron collider (CEPC) positron source has a higher frequency, as explained in [35]. However, for the new-generation SIF, PC40 was chosen because it is easy to find and cheap.

The PC40 has flux saturation of 0.5 T at 25 °C and decreases with a rising temperature, with a curies point of around 200 °C [21]. The flux saturation refers to the upper limit at which B can exist in the flux concentrator. In the authors' experience, the flux concentrator may degrade, have low efficacy, and have a short lifespan if it is used for B while exceeding the upper limit. Therefore, to select the suitable optimum model's design for PC40, we need to ensure that the B of the flux concentrator does not exceed the flux saturation of PC40. Table 6 reports the B of PC40 for various thicknesses calculated by the EA at 2200 W. From this Table, all thicknesses provided the same B_s ; however, B inside PC40 decreased with increasing thickness, as expected. Significantly, B inside PC40 was higher than the flux saturation of 0.5 T for the thickness from 1 mm to 10 mm; therefore, they are unsuitable for the SIF. For the 12 mm and 15 mm thickness, the B inside PC40 was 0.496 T and 0.357 T, not exceeding the flux saturation at 25 °C of PC40; therefore, both were suitable for the SIF. However, the 15 mm thickness is better, since it can still receive more B if the power is increased more than 2200 W. The thickness oversize of 15 mm cannot be contained in the SIF.

Table 6. The B inside PC40 for various thicknesses.

Thickness (mm)	B_s (T)	B Inside PC40 (T)	Status
1	0.219	1.254	Not suitable
5	0.219	0.994	Not suitable
7	0.219	0.841	Not suitable
10	0.219	0.602	Not suitable
12	0.219	0.469	Suitable
15	0.219	0.357	Suitable (Selected)

Figure 16 shows the sample results of Table 6 for the thickness of (a) 5 mm and (b) 15 mm calculated by the EA. It revealed that the B distribution of SIF with different thicknesses remained the same, but B inside PC40 in (a) was higher than in (b), as expected, since the thickness in (a) is thinner than in (b). Significantly, the flux concentrator in (b) is not in the upper limit of flux saturation; it can also contain more B if applied with more power. The results B inside PC40, the 3rd column, reported in Table 6, are consistent with the work of Zhang et al. [36], who employed COMSOL multiphysics to study the B in various shapes of flux concentrators. They found that reducing the size of the flux concentrator enhances the B gain inside. On the other hand, enlarging the flux concentrator reduces the B gain inside. Additionally, the status in Table 6, the 4th column, is in line with the report of Sun et al. [37] that the flux concentrator has a saturated magnetic field. Adding the B to a saturated flux concentrator will not increase its efficacy. Accordingly, references [36,37] confirm the simulation results reported in Table 6 and Figure 16.

**Figure 16.** The B inside PC40 for the thickness of (a) 5 mm and (b) 15 mm.

Compared to the works in [12,17], developing the induction heating machine for a jewelry factory, the SIF in this article is more complex than the mentioned work, challenging the authors. For example, the coils in [12,17] are single-layer, but in this article, we engage with double-layer coils. The mentioned works exclude flux concentrators and crucibles, but this article includes them.

Using Model I, PC40 with a thickness of 15 mm is a suitable design for the SIF to determine the B_s in terms of varying the power, compared to the conventional SIF. Table 7 compares the B_s of the conventional and developed SIF calculated by the EA for various powers. The value in the bracket is the percentage increment of the developed SIF compared to the conventional one. Clearly, the developed SIF is better than the conventional SIF. The maximum percentage increment was about +159% at 1000 W, confirming that the developed SIF is better than the conventional one.

Table 7. The comparison of the B_s calculated by the EA between the conventional and developed SIF.

Power (W)	B_s (T)	
	Conventional SIF	Developed SIF
1000	0.087	0.138 (+159%)
1600	0.114	0.174 (+152%)
2200	0.144	0.219 (+152%)

4.4. Limitations, Clean Technology, and SDGs

Three limitations may affect multiphysics. First, the coils' T was 25 °C as a constant, which was the ambient temperature because of the cooling water in Figure 6. Meanwhile, the actual temperature of the coils was higher due to actual use. It may rise to 60 °C and become saturated. Second, the multiphysics results reported in this article exclude the proximity and slot effects, since Equations (10) and (11) do not cover the nanoscopic or microscopic levels. Both are suitable for the macroscopic scale; therefore, the performance may differ slightly from the expectation when the improved SIF is put into production and employed. Last, since the improved SIF had higher B_s than the conventional SIF of about 150%, as reported in Table 7, the authors assume that the improved SIF used 50% less electric current than the conventional SIF to generate the same B_s . This assumption was used to estimate the expense and show the benefits of using the improved SIF, as explained in Table 8.

Since the improved SIF, powered by electricity, can produce a higher-quality glass souvenir and the raw materials are local household glass scraps, this research is considered clean technology. Its outcomes are consistent with the sustainable development goals (SDGs) of goal 9: industry, innovation, and infrastructure, and goal 12: responsible consumption and production [38].

Table 8 reports a theoretical estimation of expenses and benefits using the improved SIF compared alongside other high-temperature sources to confirm the achievement of the SDGs.

Compared with the same conditions, such as for preparing a melting glass of 0.2 kg at 1400 °C, a melting time of 12 min, an energy charge of 7.0 baht/unit, LPG of 30 baht/kg, an electric oven modeled PLF 120/27, the improved SIF was 1.5 times more efficient than the conventional SIF, and the estimated expenses could be calculated as shown below.

In the 1st row, using an electric oven with LPG consumed 0.98 of the electrical unit and 0.1 kg of LPG; the estimated expense was about 7.9 baht. Unfortunately, this method generated exhaust gases, such as CO₂, NO_x, SO_x, and minute dust, which totaled 14–26 mg [39] and were not environmentally friendly, but the two others did not. Similarly, in the 2nd row, an electric oven had the expense of 4.9 baht and did not generate exhaust gases. In the 3rd and 4th rows, implementing the conventional SIF and improved SIF had expenses of 2.24 baht and 1.12 baht, respectively, based on the last assumption mentioned above. Accordingly, the improved SIF is highly efficient, cost-saving, and environmentally friendly, achieving the SDGs.

Table 8. Theoretical estimation of expenses.

Source	Power (W)	Melting Temperature (°C)	Exhaust Gas (mg)	Unit	Estimated Expense ^a (Baht)
Electric oven ^c with LPG ^d	4900 + LPG	1400	14–26 [39]	0.98 (LPG = 0.1 kg)	7.9
Electric oven ^c	4900	1400	N/A	0.98	4.9
SIF					
Conventional	1600	1400	N/A	0.32	2.24
Improved	1600	1400	N/A	0.16 ^b	1.12 ^b

^a, using 7.0 baht/unit. ^b, supposing the improved SIF was 1.5 times more efficient than the conventional SIF. ^c, an electric oven modeled PLF 120/27. ^d, LPG: 30 baht/kg.

5. Conclusions

This article presents the successful development of the SIF for Thai SMEs' glass souvenir production process using multiphysics, aimed at recycling household glass scrap into an attractive glass souvenir, which consists of electromagnetic analysis (EA) and thermal analysis (TA). First, the experiments were set up in the laboratory to measure I , f , h , and T of SIF. Next, the I , f , and h results were employed for the EA settings. As expected, the EA results revealed B and ΔV_{Ohm} , depending on SIF design and operating conditions. Also, as expected, the TA results revealed T , which was consistent with the experimental results and confirmed the credibility of the multiphysics and methodology. Then, ferrites B, PE22, and PC40 as flux concentrator materials were added to the SIF. The EA reported that B was nearly the same, but PC40 is suitable since it is cheap and easy to find. As expected, the B is more dense in the flux concentrator than in other regions. After that, the EA was repeated by varying the PC40's thickness from 1 to 15 mm. It was found that B_s is the same, but B inside PC40 decreased with the increase in thickness. In sum, a 15 mm thickness is suitable for the developed SIF since it can contain more B generated for a higher power, while the others cannot. Lastly, the EA revealed that the developed SIF using PC40 as a flux concentrator with a thickness of 15 mm generated a B_s of 0.138 T, which was higher than the 0.087 T generated by the conventional SIF, an increase of about 159% at the power of 1000 W, and about 152% at the power of 1600 W and 2200 W. The findings of this research were applied to the development of the SIF and glass souvenir production process, which received good feedback from Thai SMEs after implementation in the production process, achieving SDGs 9 and 12.

Author Contributions: Conceptualization, J.T. and P.P.; methodology, J.T., S.S. and S.P.; software, J.T. and S.P.; validation, J.T., P.P. and S.P.; formal analysis, J.T.; investigation, J.T.; resources, S.P.; data curation, S.P.; writing—original draft preparation, J.T.; writing—review and editing, J.T. and P.P.; visualization, S.P.; supervision, J.T.; project administration, J.T.; funding acquisition, J.T. All authors have read and agreed to the published version of the manuscript.

Funding: The partial APC was funded by the College of Advanced Manufacturing Innovation, King Mongkut's Institute of Technology Ladkrabang.

Institutional Review Board Statement: Not applicable.

Informed Consent Statement: Not applicable.

Data Availability Statement: Data are contained within the article.

Acknowledgments: This research received useful information about the glass souvenir production process from the Nonghang women's economic empowerment group in the Ubon Ratchathani Geopark area in Ubon Ratchathani, Thailand. P.P. and S.S. acknowledge Thailand Science Research and Innovation (TSRI), National Science, Research and Innovation Fund (NSRF), and Ubon Ratchathani Rajabhat University (UBRU) for Fundamental Fund.

Conflicts of Interest: The authors declare no conflicts of interest.

Nomenclatures

AC	Alternating current
I	Applied current to the coil (A)
σ	Bulk conductivity (S/m)
T_c	Coil's temperature ($^{\circ}$ C)
J	Current density (A/m ²)
I_d	Eddy current (A)
d	Distance from the coil's center (m)
$\{J\}$	Electric current density matrix (A/m ³)

ρ	Density (kg/m ³)
ρ_r	Electric resistivity ($\Omega \cdot m$)
EA	Electromagnetic analysis
{Q}	External–thermal vector load (J)
h	Film convection coefficient (W/m ² °C)
f	Frequency (Hz)
k	Isotropic thermal conductivity (W/m °C)
[H]	Magnetic field matrix (T)
B	Magnetic flux density (T)
B_s	Magnetic flux density on the crucible’s surface (T)
μ	Magnetic permeability (H/m)
B_{max}	Maximum magnetic flux density (T)
{T}	Nodal vector temperature (°C)
N	Number of coil turn
ΔV_{Ohm}	Ohmic losses (W)
ϵ	Permittivity (F/m)
P	Power (W)
ϵ_r	Relative electric permittivity
k_r	Relative permeability
δ	Skin depth (m)
SIF	Small induction furnace
c	Specific heat (J/kg °C)
[S]	Stiffness matrix (A/m)
T	Temperature (°C)
TA	Thermal analysis
TC	Thermochromic
[K]	Thermal stiffness matrix (J/m °C)

References

- Rudnev, V.; Loveless, D.; Cook, R.L.; Black, M. *Handbook of Induction Heating*, 1st ed.; CRC Press: Boca Raton, FL, USA, 2002; pp. 11–97.
- Lucía, O. Induction Heating Technology and Its Applications: Past Developments, Current Technology, and Future Challenges. *IEEE Trans. Indus. Electron.* **2014**, *61*, 2509–2520. [[CrossRef](#)]
- Haimbaugh, R.E. *Practical Induction Heat Treating*, 2nd ed.; ASM International: Materials Park, OH, USA, 2015; pp. 191–210.
- Perminov, A.V.; Nikulin, I.L. Mathematical Model of the Processes of Heat and Mass Transfer and Diffusion of the Magnetic Field in an Induction Furnace. *J. Eng. Phys. Thermophys.* **2016**, *89*, 397–409. [[CrossRef](#)]
- Hadad, Y.; Kochavi, E.; Levy, A. Inductive Heating with a Stepped Diameter Crucible. *Appl. Therm. Eng.* **2016**, *102*, 149–157. [[CrossRef](#)]
- Buliński, P.; Smolka, J.; Gola, S.; Przyłucki, R.; Palacz, M.; Siwiec, G.; Lipart, J.; Białecki, R.; Blacha, L. Numerical and Experiment Investigation of Heat Transfer Process in Electromagnetically Driven Flow within a Vacuum Induction Furnace. *Appl. Therm. Eng.* **2017**, *124*, 1003–1013. [[CrossRef](#)]
- Buliński, P.; Smolka, J.; Siwiec, G.; Blacha, L.; Gola, S.; Przyłucki, R.; Palacz, M.; Melka, B. Numerical Examination of the Evaporation Process within a Vacuum Induction Furnace with a Comparison to Experimental Results. *Appl. Therm. Eng.* **2019**, *150*, 348–358. [[CrossRef](#)]
- Buliński, P.; Smolka, J.; Gola, S.; Przyłucki, R.; Palacz, M.; Siwiec, G.; Melka, B.; Blacha, L. Numerical Modelling of Multiphase Flow and Heat Transfer within an Inductive Skull Melting Furnace. *Int. J. Heat Mass Transf.* **2018**, *126*, 980–992. [[CrossRef](#)]
- Lu, L.; Zhang, S.; Xu, J.; He, H.; Zhao, X. Numerical Study of Titanium Melting by High Frequency Inductive Heating. *Int. J. Heat Mass Transf.* **2017**, *108*, 2021–2028. [[CrossRef](#)]
- García-Nichelena, P.; Ruiz-Reina, E.; Herrero-Dorca, N.; Chamorro, X. Multiphysics Modeling and Experimental Validation of Heat and Mass Transfer for the Vacuum Induction Melting Process. *Appl. Therm. Eng.* **2024**, *243*, 122562. [[CrossRef](#)]
- Jansaengsuk, T.; Pattanapichai, S.; Poopanya, P.; Phimpakarn, N.; Thongsri, J. Thermal Simulation of Microwave Kiln based on Multiphysics. In Proceedings of the International Technical Conference on Circuit/Systems, Computer, and Communications (ITC-CSCC), Jeju, Republic of Korea, 25–28 June 2023.
- Jansaengsuk, T.; Pattanapichai, S.; Thongsri, J. A Development of an Induction Heating Process for a Jewelry Factory: Experiments and Multiphysics. *Processes* **2023**, *11*, 858. [[CrossRef](#)]
- Stauffer, P.R.; Sneed, P.K.; Hashemi, H.; Phillips, T.L. Practical Induction Heating Coil Designs for Clinical Hyperthermia with Ferromagnetic Implants. *IEEE Trans. Biomed. Eng.* **1994**, *41*, 17–28. [[CrossRef](#)]

14. Khazaal, M.H.; Abdulbaqi, I.M.; Thejel, R.H. Modeling, Design, and Analysis of an Induction Heating Coil for Brazing Process using FEM. In Proceedings of the International Conference on Multidisciplinary in IT and Communication Science and Applications, Baghdad, Iraq, 9–10 May 2016.
15. Khazaal, M.H.; Abdulbaqi, I.M.; Thejel, R.H. Electromagnetic-Thermal Coupled Analysis of a Brazing Process by Induction Furnace using Finite Element Method. *J. Eng. Sustain. Devel.* **2017**, *21*, 13–25.
16. Karnaushenko, D.; Kang, T.; Schmidt, O.G. Shapeable Material Technologies for 3D Self-Assembly of Mesoscale Electronics. *Adv. Mater. Technol.* **2019**, *4*, 1800692. [[CrossRef](#)]
17. Pattanapichai, S.; Jansaengsuk, T.; Thongsri, J. A Dual Coil Induction Heating Machine for Jewelry Factories Developed by Electromagnetic Analysis. *J. Adv. Join. Process.* **2023**, *7*, 100146. [[CrossRef](#)]
18. Przyłucki, R.; Golak, S.; Buliński, P.; Smolka, J.; Palacz, M.; Siwiec, G.; Lipart, J.; Blacha, L. Analysis of the Impact of Modification of Cold Crucible Design on the Efficiency of the Cold Crucible Induction Furnace. *IOP Conf. Series Mater. Sci. Eng.* **2018**, *335*, 012009. [[CrossRef](#)]
19. Fashu, S.; Lototskyy, M.; Davids, M.W.; Pickering, L.; Linkov, V.; Tai, S.; Renheng, T.; Fangming, X.; Fursikov, P.V.; Tarasov, B.P. A Review on Crucible for Induction Melting of Titanium Alloys. *Mater. Des.* **2020**, *186*, 108295. [[CrossRef](#)]
20. Garcial-Michelena, P.; Chamorro, X.; Herrero-Dorca, N.; Bernal, D.; Hurtado, I.; Ruiz-Reina, E.; Arnesto, J.M.; Caballero, O.; Esquisabel, X.; Madariaga, I. Effect of the Crucible Composition on the Inconel 718 Vacuum Induction Melting Process Efficiency. *J. Mater. Res. Technol.* **2023**, *23*, 3351–3361. [[CrossRef](#)]
21. Rudnev, V.; Loveless, D. 12.15-Induction Hardening: Technology, Process Design, and Computer Modeling. *Compr. Mater. Process.* **2014**, *12*, 489–580. [[CrossRef](#)]
22. Nian, S.C.; Huang, M.S.; Tsai, T.H. Enhancement of Induction Heating Efficiency on Injection Mold Surface using a Novel Magnetic Shielding Method. *Int. Commun. Heat Mass Transf.* **2014**, *50*, 52–60. [[CrossRef](#)]
23. Im, S.H.; Kim, J.S.; Jang, Y.S.; Park, G.S. Design of Ferite Core for the Improvement of Power Efficiency in Induction Range. *IEEE Trans. Magn.* **2019**, *55*, 8001304. [[CrossRef](#)]
24. Thai SMEs and Their Mission to Create Economic Stability under Trends of Change. Available online: <https://tdri.or.th/2023/09/economic-sme-article/v> (accessed on 29 February 2024). (In Thai).
25. Sriphalang, S.; Saenkham, A.; Chaodongbung, T.; Wannoo, B.; Kaewtong, C.; Pattavarakorn, D. Reversible Coloring/Decoloring Reactions of Thermochromic Leuco Dyes Controlled by a Macrocyclic Compound Developer. *Structural Chemistry* **2022**, *33*, 1085–1095. [[CrossRef](#)]
26. Lecture 1: Introduction to ANSYS Maxwell. In *ANSYS Maxwell V16 Training Manual*; ANSYS Inc.: Canonsburg, PA, USA, 2013.
27. Lesson 4: Intro to Heat Transfer in Fluids. In *Key Concepts in Thermal Conduction*; ANSYS Inc.: Canonsburg, PA, USA, 2020.
28. Thongsri, J.; Srathonghuam, K.; Boonpan, A. Gas Flow and Ablation of 122 Supersonic Rocket Nozzle Investigated by Conjugate Heat Transfer Analysis. *Processes* **2022**, *10*, 1823. [[CrossRef](#)]
29. Lecture 6: Meshing and Mesh Operations. In *ANSYS Maxwell V16 Training Manual*; ANSYS Inc.: Canonsburg, PA, USA, 2013.
30. Ashby, M. *Material Property Data for Engineering Materials*, 5th ed.; ANSYS Inc.: Canonsburg, PA, USA, 2021.
31. Mn-Zn Ferrite Material Characteristics. Available online: https://product.tdk.com/en/system/files?file=dam/doc/product/ferrite/ferrite/ferrite-core/catalog/ferrite_mn-zn_material_characteristics_en.pdf (accessed on 21 March 2024).
32. Patidar, B.; Hussain, M.M.; Jha, S.K.; Sharma, A.; Tiwari, A.P. Analytical, Numerical and Experimental Analysis of Induction Heating of Graphite Crucible for Melting Non-Magnetic Materials. *IET Electr. Power Appl.* **2017**, *11*, 342–351. [[CrossRef](#)]
33. Thakur, P.; Chahar, D.; Taneja, S.; Bhalla, N.; Thakur, A. A Review on MnZn Ferrites: Synthesis, Characterization and Applications. *Ceram. Int.* **2020**, *46*, 15740–15763. [[CrossRef](#)]
34. Liu, J.D.; Li, X.P.; Meng, C.; Chi, Y.L.; Pei, G.X.; He, D.Y.; Li, J.Y.; Sun, X.J.; Zhang, J.R.; Shang, L.; et al. System Design and Measurements of Flux Concentrator and Its Solid-State Modulator for CEPC positron source. *Nuc. Sci. Tech.* **2021**, *32*, 77. [[CrossRef](#)]
35. Kaçki, M.; Ryłko, M.S.; Hayes, J.G.; Sullivan, C.R. Measurement Method for High-Frequency Characterizations of Permeability, Permittivity, and Core Loss of Mn-Zn Ferrite Cores. *IEEE Trans. Power Electron.* **2022**, *37*, 15152–15162. [[CrossRef](#)]
36. Zhang, X.; Bi, Y.; Chen, G.; Liu, J.; Li, J.; Feng, K.; Lv, C.; Wang, W. Influence of Size Parameters and Magnetic Field Intensity upon the Amplification Characteristics of Magnetic Flux Concentrators. *AIP Adv.* **2018**, *8*, 125222. [[CrossRef](#)]
37. Sun, X.; Jiang, L.; Pong, P.W.T. Magnetic Flux Concentration at Micrometer Scale. *Microelectron. Eng.* **2013**, *111*, 77–81. [[CrossRef](#)]
38. United Nations Development Programme. What Are the Sustainable Development Goals. Available online: <https://www.undp.org/sustainable-development-goals> (accessed on 25 March 2024).
39. Adewole, B.Z.; Abidakun, O.A.; Asere, A.A. Artificial Neural Network Prediction of Exhaust Emissions and Flame Temperature in LPG (Liquefied Petroleum Gas) Fueled Low Swirl Burner. *Energy* **2013**, *61*, 606–611. [[CrossRef](#)]

Disclaimer/Publisher’s Note: The statements, opinions and data contained in all publications are solely those of the individual author(s) and contributor(s) and not of MDPI and/or the editor(s). MDPI and/or the editor(s) disclaim responsibility for any injury to people or property resulting from any ideas, methods, instructions or products referred to in the content.